The published version is available via https://doi.org/10.1109/JSEN.2019.2910585

Highly Sensitive Refractive Index Sensor using Dual Resonance in Subwavelength Grating/Waveguide with Normally Incident Optical Geometry

Yuusuke Takashima, *Member, IEEE,* Keita Kusaba, Masanobu Haraguchi, and Yoshiki Naoi, *Member, IEEE*

***Abstract*—A highly sensitive refractive index sensor with normally incident optical geometry was experimentally demonstrated using dual resonance in a subwavelength grating (SWG) on a waveguide. Two eignemodes within the SWG and waveguide were utilized for refractive index sensing with the reduction of noise such as background noise. The finite-difference time-domain numerical method was used to estimate the refractive index sensing performance of our sensor. The calculated electric field clarified that the incident light could excite modes in the SWG and waveguide with normally incident optical geometry, and the modes formed two resonance reflection peaks. The calculation showed that these dual resonance peaks depended differently on the refractive index of the ambient around the sensor, and the intensity difference between both resonance peaks varied with the slight change in refractive index of the ambient. The sensor was fabricated using traditional electron-beam lithography techniques, and two reflection resonant peaks were experimentally obtained. The difference between the dual resonance peak intensities varied significantly with the minuscule change in refractive index of the ambient around the sensor, and the resolution of the refractive index reached 7.65×10^{-4}, assuming a spectrometer intensity sensitivity of 1%.**

***Index Terms*—Refractive index sensor, subwavelength grating, waveguide.**

I. Introduction

Highly sensitive refractive index (RI) sensors have been widely used in many applications such as bioassay and gas detection [1]. Integrated RI sensors can open new fields of integrated applications in Internet of Things (IoT) devices, such as blood sensing, cancer detection, and portable health meters. To realize these integrated applications, high-sensitivity, compactness, real-time sensing, and ease of handling without any special techniques are highly desirable.

Optical RI sensors are very useful for the IoT applications mentioned above owing to their advantages such as rapid response and immunity to electromagnetic interference. Extremely-high-sensitivity RI sensors have been achieved using surface plasmon polaritons (SPPs) at the boundary between metals and dielectrics [1] [2] [3] [4]. The SPPs are coupled with the incident light when the wavenumbers of both waves match. The wavenumber of the SPP strongly reflects the RI values of the metal and dielectric, and the RI value of the dielectric near the boundary is sensitively detected. Although SPP sensors have achieved extremely high sensitivities, a prism coupler, which is too bulky for integrated devices, is generally necessary to increase the wavenumber of the incident light because the wavenumber of SPPs is always larger than that of light in free-space. Other optical RI sensors using no prism couplers have also been developed using metal nanoparticles [5], metal nanorings [6] [7], ring resonators [8] [9], photonic crystals [10] [11] [12], optical microfibers [13], and nanogratings [14] [15] [16] [17] [18] [19]. Compact device sizes are quite suitable for integrated sensing applications. However, the use of theses sensors is restricted by the noise and environment around the measurement system, for example, the intensity fluctuation of the light source and variation in the background noise level.

Recently, RI sensing techniques utilizing dual resonance in erbium-doped optical fibers and double-layer metal gratings have been investigated [20] [21]. The RI sensing techniques are based on dual-resonance dips (or peaks) in its transmission (or reflection) spectra, and the reliability and temporal stability of these sensors have been significantly improved because the influence of the fluctuation of the light source and background noise level can be cancelled out using the difference in output intensities between these resonances. Although the dual-resonance-based RI sensors possess these advantages, the cumbersome fabrication process, high cost, and complex measurement system are still problems, for example, the nano-structure fabrication on both sides of a thin film [20].

In this article, we theoretically and experimentally

This work was partially supported in part by JSPS KAKENHI Grant Number JP18K04238 and LED general platform project of Tokushima University.
Y. Takashima, M. Haraguchi, and Y. Naoi are with Graduate School of Technology and Social Science, Tokushima University, 2-1 Minami-josanjima, Tokushima 770-8506, Japan (e-mail: takashima@ee.tokushima-u.ac.jp)

demonstrate a dual-resonance-based RI sensor using a subwavelength grating (SWG)/waveguide structure fabricated using the traditional lithography process. The electromagnetic field distribution calculated using the finite-difference time-domain (FDTD) method indicates that our proposed sensor can measure the minuscule changes in RI of an ambient by a very simple optical incidence system. The SWG/waveguide structure was fabricated using traditional electron-beam (EB) lithography techniques, and highly sensitive RI sensing was experimentally and successfully achieved using the dual resonance in the structure.

II. Design of Subwavelength Grating/Waveguide for RI Sensor

In this section, we explain the operation principle of our proposed RI sensor and present the design of the SWG/waveguide structure for RI sensing. Fig. 1 shows a schematic of our proposed SWG/waveguide structure. The SWG, whose period is shorter than the incident wavelength in free space, is placed on top of the clad/core/substrate waveguide structure. The structural parameters, such as grating period, grating ridge width, grating height, clad thickness, and core thickness, correspond to the symbols Λ, w, t_{SWG}, t_{clad}, and t_{core} in Fig. 1, respectively.

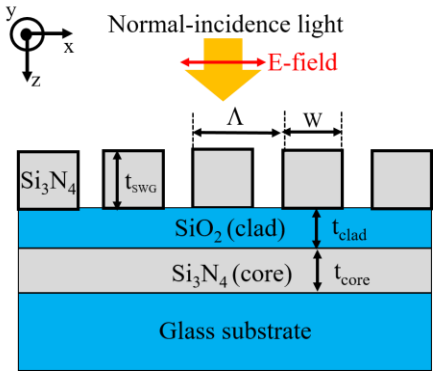

Fig. 1. Schematic of SWG/waveguide structure.

We assume that the p-polarized incident light, whose electric field is perpendicular to the grating stripe (red arrow in Fig. 1), is normally incident on our structure. When the light is incident on our structure, only the zeroth diffraction orders (transmission and reflection) carry the energy of the light, while the other, higher diffraction orders cannot; in other words, the higher diffraction orders are evanescent. In this case, two resonances can occur in our structure in certain conditions. One can be found in the SWG structure and the other can be obtained in the waveguide structure. Inside the SWG, its periodic RI distribution induces sets of Bloch eigenmodes as solutions to Maxwell's equations. In particular, a high RI contrast between the grating and the ambient excites not only the fundamental eigenmode but also the higher-order eigenmodes [22] [23]. The excited eigenmodes interfere with each other during the round trip along the SWG, and the interference determines the optical responses of the SWG structure, such as transmission and reflection [23]. The transmission coefficient of the zeroth diffraction order τ_0 is given by [22] [23] [24]

$$\tau_0 = \left(\eta\gamma_0/k_0\right)^{-2} \sum_m \left(a_m + a_m^{\rho}\right) \Lambda^{-1} \int_0^{\Lambda} f_m(x)dx. \quad (1)$$

Where, the symbols k_0 γ_0 η are the wavenumber of the incident light, the wavenumber of the zeroth diffraction order, and the impedance of vacuum, respectively. The symbols of a_m and a^{ρ}_m represent the coefficients of the forward ($+z$) and backward ($-z$) propagating modes. The subscript m is order of the mode in the SWG. The function $f_m(x)$ is lateral (x-direction) field profile of the mode at the interface between SWG and SiO_2. According to (1), the average lateral field among the period Λ determines the transmittance coefficient of the zeroth diffraction order. If the eigenmodes destructively interfere to cancel out the zeroth transmitted diffraction order, the energy of the incident light fully returns back [24] [25] [26] [27] [28] [29] [30]. As a result, a resonance peak is obtained in the reflection spectra of our structure.

Another resonance is obtained in the clad/core/substrate waveguide structure shown in Fig. 1. Waveguide modes can be coupled with higher-order diffractions (we consider first-order diffraction in this work) by the SWG when the wavenumber matching conditions between both are satisfied [18] [31] [32] [33] [34] [35]. During waveguide mode propagation along the core layer, a part of the excited waveguide modes is reradiated by the SWG into the incident side. When the reradiated waves are in-phase with the reflected zeroth diffraction order, constructive interference occurs between both waves. As a result, a sharp peak appears in its reflection spectra.

The conditions of these resonances vary with the change in RI value of the ambient around the structure because the wavenumbers of the eigenmodes in the SWG and in the waveguide strictly depend on the ambient RI. Thus, the reflection intensities at these resonances vary depending on the RI value of the ambient. We also expect the resonances to have a different dependence on the RI value of the ambient because the SWG is directly surrounded by the ambient while the waveguide is not. Hence, the intensity difference between the resonances also changes the RI value of the ambient.

Based on the sensing principles mentioned above, we designed the SWG/waveguide structure for RI sensing. First, we selected visible light from about 400 to 600 nm as the wavelengths of the incident light owing to their low absorption in water and ease of experimentation, because RI sensors are often used in aqueous environments. For the resonance in the SWG, a high RI contrast between the grating and surrounding material is necessary to excite higher-order Bloch eigenmodes [22] [23]. We employed Si_3N_4 as the SWG material because of its suitable RI value (Si_3N_4 RI value is about 2 around visible wavelength region) for the excitation of the higher-order modes and very low absorption coefficient in the visible region [36]. In addition, the SiO_2/Si_3N_4/optical glass substrate (D 263 T eco Thin Glass: SCHOTT) was chosen as the clad/core/clad waveguide structure. The RI values of SiO_2 were taken from the literature [37]. The SWG was designed to obtain reflection peak spectra in the visible wavelength region using the wavenumber

dispersion relation, which defines the phase of eigenmodes in the SWG [23] [24]. The waveguide structure was also designed to match the wavenumber of the waveguide mode with that of the first-order diffracted light in the visible wavelength region [18] [32]. The designed structural geometries were set to Λ = 300 nm, w = 210 nm, t_{SWG} = 210 nm, t_{clad} = 40 nm, and t_{core} = 100 nm.

We numerically calculated the electromagnetic field distribution in our designed structure using the FDTD method (Fullwave: Rsoft, Synopsys) in order to estimate the RI sensing performance of our sensor. The cross-section of the calculation model is illustrated in Fig. 2. In this model, the Si_3N_4-SWG was placed on the SiO_2/Si_3N_4/optical glass waveguide structure. The SWG was surrounded by ambient, with n_a being the RI value. We assumed that the model size for the y-direction was infinite because the length of our actual structure along the y-direction was much larger than the incident wavelength.

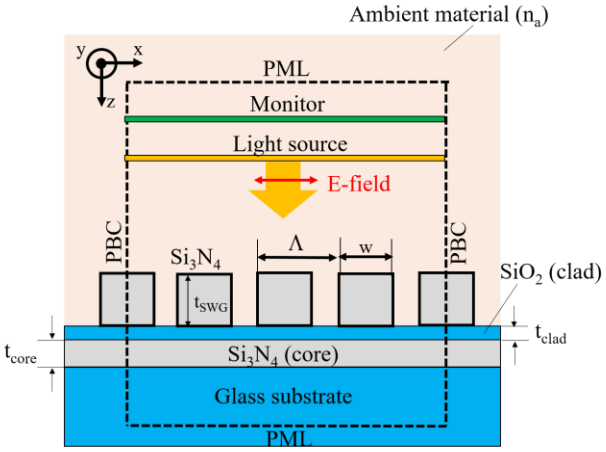

Fig. 2. Cross-section of FDTD calculation model.

We also considered an infinite number of grating stripes and employed a periodic boundary condition (PBC), for the x-direction. Under PBC, the electric and magnetic field of the light are given by

$$F(x) = F(x + \Delta) \quad (2).$$

Here, $F(x)$ in (2) are the electric or the magnetic field of the light, and the fields infinitely repeat with period Δ. The symbol Δ is defined by the length of the calculation region for x-direction. A perfectly matched layer (PML), was applied as the boundary condition for the z-direction. PML boundary was defined as a highly lossy material, and all energy of the light entering into the PML is perfectly aborted. The impedance of PML was also adjusted to occur no reflection at the boundary. The dashed lines in Fig. 2 indicate each boundary, and the square area surrounded by the boundaries represents the calculation region. To converge the numerical FDTD calculation, the spatial grid and incremental time interval were set to 2 nm and 4.6 x 10^{-13} s, respectively. The light source was placed at the upper structure. A p-polarized plane wave with its electric field perpendicular to the grating stripe was normally incident on the SWS/waveguide structure. The monitor, in which the Poynting vector of the electromagnetic field was calculated, was placed behind the light source. The magnitude of Poynting vector is defined as

$$S(r,t) = [E(r,t)H(r,t)]. \quad (3)$$

Where, $S(r, t)$ is magnitude of Poynting vector, and the $E(r, t)$ and $H(r, t)$ indicate the electric and magnetic field of the light. The symbol r and t are spatial coordinate and time, respectively. We calculated the reflected intensity at the monitor via the Poynting vector when the value of n_a varied.

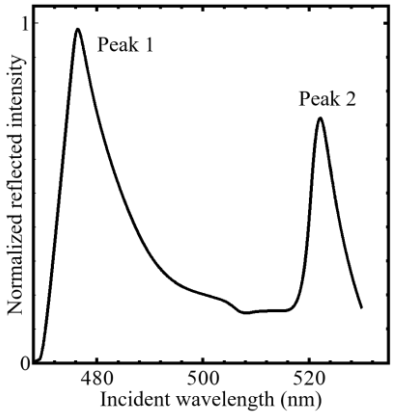

Fig. 3. Normalized reflection spectra of the SWG/waveguide at n_a = 1.336.

Fig. 3 presents the normalized reflection spectra of the SWG/waveguide at n_a = 1.336. The case of n_a = 1.336 corresponds to pure water ambient around the structure [38]. As shown in Fig. 3, dual reflection peaks are obtained at 476 nm (Peak 1) and 522 nm (Peak 2). Fig. 4 illustrates the dependence of the intensity difference between Peak 1 and Peak 2 on n_a. The range of n_a in the calculation are 1.336 to 1.35.The intensity difference is also normalized by the intensity of Peak 1, so it indicates the relative intensity difference with respect to the intensity of Peak 1. The dashed line is the least-squares method fit.

As shown in Fig. 4, the intensity difference increases with the n_a value, and we find two inclination regions for the change in n_a. We consider that these different inclinations can be attributed to the nonlinear dependence of the wavenumber dispersion relation of the Bloch eigenmode and waveguide mode [23] [24] [32]. In the high-sensitivity region (white region in Fig. 4), the calculation result indicates that the change in intensity difference per refractive index unit (RIU) reaches 1233 %/RIU, and this sensitivity indicates that our sensor can measure a change of 8.11 × 10^{-4} RIU with a very simple normal-incidence system, assuming the spectrometer intensity sensitivity is 1%.

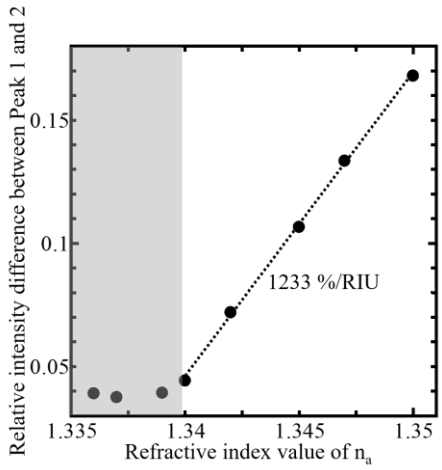

Fig. 4. Dependence of the relative intensity difference between Peak 1 and Peak 2 on n_a.

To provide deep insight into the dependence of these resonances on n_a, the calculated electric field distributions around the SWG/waveguide structure are presented in Fig. 5. Figs. 5 (a) and (b) show the electric field distribution for the x-component (E_x) at Peak 1 and Peak 2 with n_a = 1.336 at a certain time, respectively. The green squares represent the grating bars. The yellow square represents the light source. Only reflected light from the SWG/waveguide structure exists in the area above the light source. The field amplitudes were normalized by those of the incident light. For Peak 1, an about 2.3-times greater E_x than that of the incident light exists in the SWG. The amplitude in the grating bar and air gap is out-of-phase and cancels each other out to make the average of the E_x field nearly zero. This implies that the eignemodes in the SWG performed destructive interference at the bottom of the SWG. As a result, the transmitted field amplitude is very low, and most of the incident light reflects back. This condition corresponds to the low transmission condition of the SWG [23] [24], and this result indicates that Peak 1 is attributed to the resonance in the SWG.

In contrast, the amplitude of the E_x component at Peak 2 is much lower than that in the case of Peak 1, as shown in Fig. 5 (b). The amplitude of E_x in the grating bar and air gap is in-phase, which indicates that constructive interference, which leads to a highly transmitted light intensity, occurs at the bottom of the SWG. However, the transmitted light intensity is low, and the reflected intensity becomes high. We show the electric field distribution for the z-component (E_z) in Fig. 5 (c) to investigate this highly reflected intensity at Peak 2. For the case of Peak 2, an about 14-times greater E_z component than that of the incident light exists in the waveguide structure despite the fact that the incident light propagates along the z-direction. This implies that the higher-order evanescent diffraction couples with the waveguide mode, which propagates along the x-direction. A part of the excited waveguide mode reradiates into the incident side by the SWG. The phase of the reflected light (zeroth diffraction order) and the reradiated waves is in-phase and reinforces each other (see the region above the light source in Fig. 5 (b)). As a result, a reflection peak is obtained and these results indicate that Peak 2 is attributed to the waveguide mode. The calculation results also reveal the difference in the dependence of these resonances on n_a. The SWG is directly surrounded by the material with n_a, while the waveguide structure is separated from the ambient by the SiO_2 clad layer. Thus, the dependences of Peak 1 and Peak 2 on n_a are different, and the RI sensing can be demonstrated using the intensity difference between these peaks.

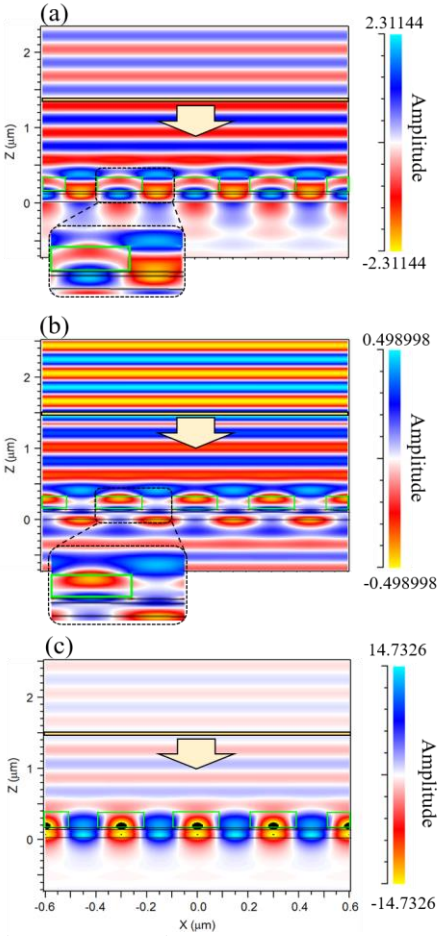

Fig. 5. Electric field distribution of (a) x-component at Peak 1, (b) x-component at Peak 2, and (c) z-component at Peak 2 with n_a = 1.336 at a certain time. The amplitude of the fields has been normalized to that of the light source.

III. Experimental Results and Discussion

The proposed SWG/waveguide structure was fabricated using the traditional EB lithography technique to demonstrate RI sensing by dual resonance. The fabrication processes are illustrated in Fig. 6.

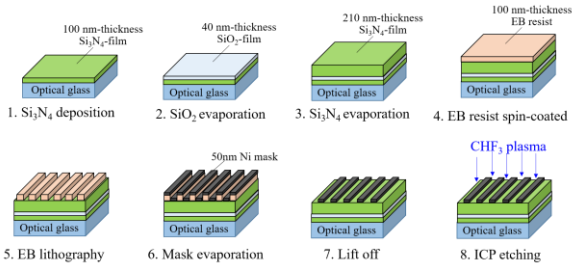

Fig. 6. Fabrication processes of the SWG/wavelength structure.

First, the Si_3N_4 film with a thickness of 100 nm was deposited on the optical glass substrate using chemical vaper deposition techniques. A 40-nm SiO_2-film was evaporated on the Si_3N_4-film, and a 210-nm Si_3N_4 film was also chemically deposited on the SiO_2 film. After that, EB resist film (ZEP520A: Zeon) with a thickness of 100 nm was spin-coated, and the sample was baked at 120 ℃ for 30 min. The grating pattern was drawn into the surface of the resist film by EB lithography, and the pattern was developed at 20 ℃ (ZED50N: Zeon). Next, Ni film with a thickness of 50 nm was evaporated onto the developed grating pattern as a metal mask for chemical etching. Inductively coupled plasma (ICP) etching with CHF_3 gas was employed to form the Si_3N_4 SWG, and the Ni mask was finally removed by diluted nitric acid. Fig. 7 shows a scanning electron microscope (SEM) image of the sample surface. The fabricated sample possesses a 300-nm grating period and 210-nm grating width, and the fabricated structural area size is 300 μm × 300 μm.

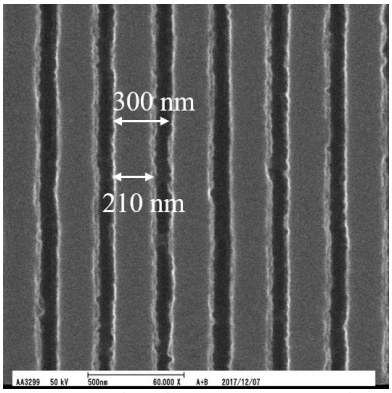

Fig. 7. SEM image of the fabricated sample surface

The normal reflection spectra of the fabricated sample were measured when the RI value of the ambient around the structure was changed. The measurement system is illustrated in Fig. 8, where the dashed region shows the measurement system around the sample in detail. Light from a halogen lamp was collimated by a plano-convex lens, and the light was p-polarized. The p-polarized light was focused on the sample surface using an objective lens (×20 NA: 0.46). The irradiated area was about 100 μm × 100 μm. The sample was placed in a plastic cell, which was filled with pure water. To evaluate the RI sensing performance, reflection spectra from the sample were measured using a spectrometer (USB4000: Ocean Optics) when ethanol was added into the pure water. Reflection at the bottom of the plastic cell was prevented by a blacked Al film placed under the cell. The measurement have been done at room temperature.

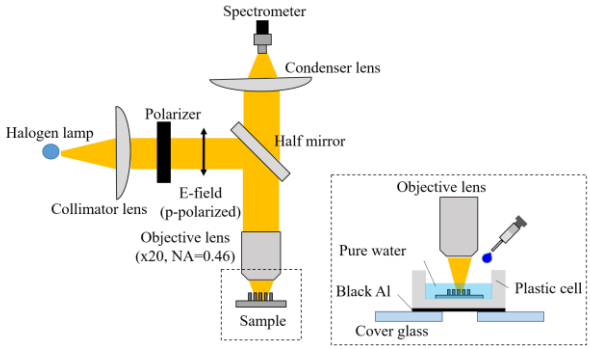

Fig. 8. Measurement system. The area surrounded by dashed lines shows details of the measurement system around the sample.

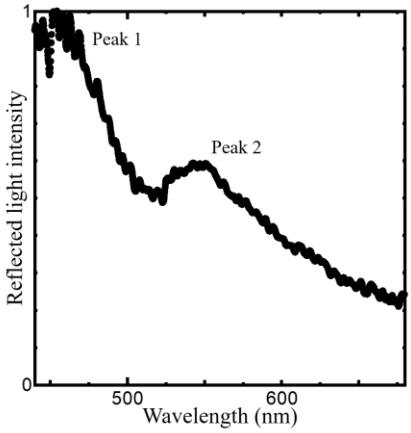

Fig. 9. Normalized reflection spectra from the fabricated sample surrounded by pure water.

Fig. 9 shows the normalized reflection spectra from the fabricated sample surrounded by pure water. We can find dual reflection peaks at wavelengths of 455 nm (Peak 1) and 544 nm (Peak 2), and these peak positions show good agreement with the calculation results. However, the reflected intensity at Peak 2 is significantly lower than that at Peak 1 compared to the calculation results. We considered that the lower intensity of peak 2 is attributed to the fabrication error of the SWG. The actually fabricated sample contains a fabrication error, such as a nonideal rectangular grating and a fluctuation in grating bar width (see Fig. 7), whereas the calculation model assumes an ideal structural shape. The fluctuation in structural geometry of the fabricated sample relaxes the resonance conditions because the wavenumbers of the Bloch and waveguide modes were broadened because of the disorder of the periodicity of the SWG. Especially, the resonance in the waveguide (Peak 2) is considerably influenced by the fabrication error, because this resonance condition requires that all reradiated waves from the waveguide are in-phase to the zeroth diffraction order [18].

Thus, the intensity of Peak 2 significantly deviates from that in the FDTD calculation model.

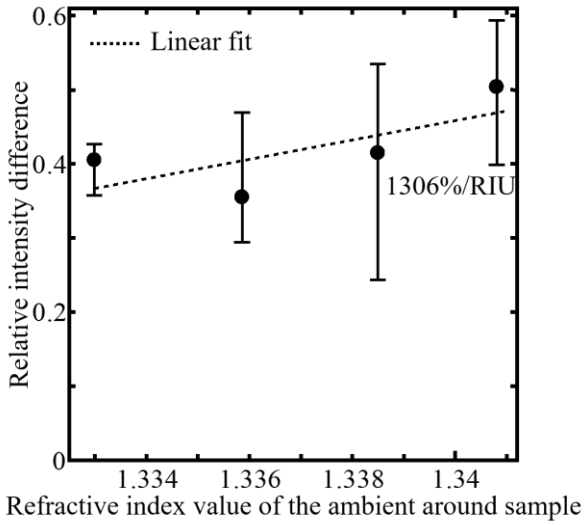

Fig. 10. Dependence of relative intensity difference between Peak 1 and Peak 2 on the refractive index values of the ambient around the sample. The refractive index values were measured by using refractometer. The error bars show the error range among three measurements. The dashed line represents a linear fit by the least-squares method.

Figure 10 also illustrates the dependence of the relative intensity difference between these peaks on the refractive index value of the ambient around the sample. The refractive index values in Fig. 10 were experimentally measured using a refractometer. The data in Fig. 10 are average value during three measurements. The error bars also show the error range among the three measurements, and we confirm the repeatability of the refractive index measurement. The dashed line in Fig. 10 shows the linear fitting by the least-squares method for rough evaluation of the sensitivity. The intensity difference was also normalized by the intensity of the peak at the wavelength of 455 nm. In the case of pure water ambient (ethanol concentration of 0), the intensity difference between the two reflection peaks is about 40%, and the difference increases with the ethanol concentration. This experimental tendency of the dependence on n_a coincides with the calculated results. The intensity change per RIU reaches 1306 %/RIU. This indicates that a change of 7.65×10^{-4} RIU can be measured with a very simple and compact optical system when we assume that the optical measurement system can detect a 1% intensity difference.

This sensitivity is higher than the calculated FDTD. This can be explained as follows. The resonance condition in the waveguide is strongly influenced by the broadening of the wavenumber of the waveguide modes because of the fabrication error. The wavenumber broadening degrades the sensitivity of the waveguide resonance for the change in the ambient, while the fabrication error has a weaker effect on the SWG resonance [39]. Thus, the intensity difference between Peak 1 and Peak 2 becomes high compared to that in the calculation.

The sensitivity of our RI sensor is comparable to other RI sensors that use photonic crystals [11], gratings [14] [16] [17], and optical fibers [21]. Moreover, our sensor in this work does not require a cumbersome fabrication process, complex optical system, or specialized techniques. Thus, our sensor has great potential for use in integrated RI sensing applications in IoT devices owing to its simple fabrication, compact device size, and ease of handling.

IV. Conclusion

We proposed and successfully demonstrated a high-sensitivity RI sensor using dual resonance in a SWG/waveguide structure. The calculated electric field indicated that the proposed SWG/waveguide structure can measure a minuscule RI change with a very simple normal-incidence system. The SWG/waveguide structure was fabricated on an optical glass substrate using the traditional EB lithography technique, and the reflection spectra from the fabricated sample exhibited dual-resonance reflection peaks in visible wavelength region. The intensity difference between these peaks varied significantly with the increase in ethanol concentration in the pure water ambient around the sample. This result demonstrates that our sensor can be practically used in integrated sensing applications for IoT devices owing to its high sensitivity, simple fabrication, compact device size, and ease of handling.

References

[1] J. Homola, S. S. Yee, and G. Gauglitz, "Surface plasmon resonance sensors: review," *Sens. Actuators B*, vol. 54, no. 1–2, pp. 3–15, Jan. 1999.

[2] R. Slavík, J. Homola, and J. Čtyroký, "Miniaturization of fiber optic surface plasmon resonance sensor," *Sens. Actuators B*, vol. 51, no. 1–3, pp. 311–315, Aug. 1998.

[3] D. Monzón-Hernández and J. Villatoro, "High-resolution refractive index sensing by means of a multiple-peak surface plasmon resonance optical fiber sensor," *Sens. Actuator B*, vol. 115, no. 1, pp. 227–231, May 2006.

[4] D. Michel, F. Xiao, and K. Alameh, "A compact, flexible fiber-optic surface plasmon resonance sensor with changeable sensor chips," *Sens. Actuator B*, vol. 246, pp. 258–261, July 2017.

[5] K. M. Mayer and J. H. Hafner, "Localized surface plasmon resonance sensors," *Chem. Rev.*, vol. 111, no. 6, pp. 3828–3857, June 2011.

[6] J. Aizpurua, P. Hanarp, D. S. Sutherland, M. Käll, G. W. Bryant, and F. J. G. de Abajo, "Optical properties of gold nanorings," *Phys. Rev. Lett.*, vol. 90, no. 5, Art. no. 057401, Feb. 2003.

[7] E. M. Larsson, J. Alegret, M. Käll, and D. S. Sutherland, "Sensing characteristics of NIR localized surface plasmon resonances in gold nanorings for application as ultrasensitive biosensors," *Nano Lett.*, vol. 7, no. 5, pp. 1256–1263, Apr. 2007.

[8] J. Flueckiger, S. Schmidt, V. Donzella, A. Sherwali, D. M. Ratner, L. Chrostowski, and K. C. Cheung, "Sub-wavelength grating for enhanced ring resonator biosensor," *Opt. Express*, vol. 24, no. 14, pp. 15672–15686, July 2016.

[9] Z. Tu, D. Gao, M. Zhang, and D. Zhang, "High-sensitivity complex refractive index sensing based on Fano resonance in the subwavelength grating waveguide micro-ring resonator," *Opt. Express*, vol. 25, no. 17, pp. 20911–20922, Aug. 2017.

[10] A. D. Falco, L. O'Faolain, and T. F. Krauss, "Chemical sensing in slotted photonic crystal heterostructure cavities," *Appl. Phys. Lett.*, vol. 94, no. 6, Art. no. 063503, Feb. 2009.

[11] Y. Liu and H. W. M. Selemink, "Photonic crystal-based all-optical on-chip sensor," *Opt. Express*, vol. 20, no. 18, pp. 19912–19920, Aug. 2012.
[12] X.-J. Tan and X.-S. Zhu, "Optical fiber sensor based on Bloch surface wave in photonic crystals," *Opt. Express*, vol. 24, no. 14, pp. 16016–16026, July 2016.
[13] K. Li, T. Zhang, G. Liu, N. Zhang, M. Zhang, and L. Wei, "Ultrasensitive optical microfiber coupler based sensors operating near the turning point of effective group index difference," *Appl. Phys. Lett.*, vol. 109, no. 10, Art. no. 101101, Sept. 2016.
[14] P. K. Sahoo, J. Joseph, R. Yukino, and A. Sandhu, "High sensitivity refractive index sensor based on simple diffraction from phase grating," *Opt. Lett.*, vol. 41, no. 9, pp. 2101–2104, May 2016.
[15] T. Sun, S. Kan, G. Marriott, and C. Chang-Hasnain, "High-contrast grating resonators for label-free detection of disease biomarker," *Sci. Rep.*, vol. 6, Art. no. 27482, June 2016.
[16] G. J. Triggs, Y. Wang, C. P. Reardon, M. Fischer, G. J. O. Evans, and T. F. Krauss, "Chirped guided-mode resonance biosensor," *Optica*, vol. 4, no. 2, pp. 229–234, Feb. 2017.
[17] A. Shakoor, M. Grande, J. Grant, and D. R. S. Cumming, "One-dimensional silicon nitride grating refractive index sensor suitable for integration with CMOS detectors," *IEEE Photonics J.*, vol. 9, no. 1, Art. no. 6800711, Feb. 2017.
[18] P. K. Sahoo, S. Sarkar, and J. Joseph, "High sensitivity guided-mode-resonance optical sensor employing phase detection," *Sci. Rep.*, vol. 7, Art. no. 7607, Aug. 2017.
[19] Y. Takashima, M. Haraguchi, and Y. Naoi, "High-sensitivity refractive index sensor with normal incident geometry using a subwavelength grating operating near the ultraviolet wavelength," *Sens. Actuator B*, vol. 255, no. 2, pp. 1711–1715, Feb. 2018.
[20] Y. Liang, W. Peng, R. Hu, and M. Lu, "Symmetry-reduced double layer metallic grating structure for dual-wavelength spectral filtering," *Opt. Express*, vol. 22, no. 10, pp. 11633–11645, May. 2014.
[21] S. Wang, S. Liu, W. Ni, S. Wu, P. Lu, "Dual-wavelength highly-sensitive refractive index sensor," *Opt. Express*, vol. 25, no. 13, pp. 14389–14396, June 2017.
[22] C. J. Chang-Hasnain, "High-contrast grating as new platform for integrated optoelectronics," *Semicond. Sci. Technol.*, vol. 26, no. 1, Art. no. 014043, Jan. 2011.
[23] C. J. Chang-Hasnain and W. Yang, "High-contrast grating for integrated optoelectronics," *Adv. Opt. Photonics*, vol. 4, no. 3, pp. 379–440, Sept. 2012.
[24] V. Karagodsky, F. G. Sedgwick, and C. J. Chang-Hasnain, "Theoretical analysis of subwavelength high contrast grating reflectors," *Opt. Express*, vol. 18, no. 16, pp. 16973–16988, Aug. 2010.
[25] C. F. R. Mateus, M. C. Y. Huang, Y. Deng, A. R. Neureuther, and C. J. Chang-Hasnain, "Ultrabroadband mirror using low-index cladded subwavelength grating," *IEEE Photonics Technol. Lett.*, vol. 16, no. 2, pp. 518–520, Feb. 2004.
[26] Y. Zhou, M. Moewe, J. Kern, M. C. Y. Huang, and C. J. Chang-Hasnain, "Surface-normal emission of a high-Q resonator using a subwavelength high-contrast grating," *Opt. Express*, vol. 16, no. 22, pp. 17282–17287, Oct. 2008.
[27] W. Hofmann, C. Chase, M. Müller, Y. Rao, C. Grasse, G. Böhm, M.-C. Amann, and C. J. Chang-Hasnain, "Long-wavelength high contrast grating vertical-cavity surface-emitting laser," *IEEE Photonics J.*, vol. 2, no. 3, pp. 415–422, June 2010.
[28] T. T. Wu, Y. C. Syu, S. H. Wu, W. T. Chen, T. C. Lu, S. C. Wang, H. P. Chiang, and D. P. Tsai, "Sub-wavelength GaN-based membrane high contrast grating reflectors," *Opt. Express*, vol. 20, no. 18, pp. 20551–20557, Aug. 2012.
[29] Y. Laaroussi, C. Chevallier, F. Genty, N. Fressengeas, L. Cerutti, T. Taliercio, O. Gauthier-Lafaye, P. F. Calmon, B. Reig, J. Jacquet, and G.Almuneau, "Oxide confinement and high contrast grating mirrors for mid-infrared VCSELs," *Opt. Mater. Express*, vol. 3, no. 10, pp. 1576–1585, Oct. 2013.
[30] M. Gębski, M. Dems, A. Szerling, M. Motyka, L. Marona, R. Kruszka, D. Urbańczyk, M. Walczakowski, N. Palka, A. Wójcik-Jedlińska, Q. J. Wang, D. H. Zhang, M. Bugajski, M. Wasiak, and T. Czyszanowski, "Monolithic high-index contrast grating: a material independent high-reflectance VCSEL mirror," *Opt. Express*, vol. 23, no. 9, pp. 11674–11686, May 2015.
[31] S. S. Wang and R. Magnusson, "Theory and applications of guided-mode resonance filters," *Appl. Opt.*, vol. 32, no. 14, pp. 2606–2613, May 1993.
[32] C.-H. Park, Y.-T. Yoon, and S.-S. Lee, "Polarization-independent visible wavelength filter incorporating a symmetric metal-dielectric resonant structure," *Opt. Express*, vol. 20, no. 21, pp. 23769–23777, Oct. 2012.
[33] M. J. Uddin and R. Magnusson, "Highly efficient color filter array using resonant Si_3N_4 gratings," *Opt. Express*, vol. 21, no. 10, pp. 12495–12506, May 2013.
[34] D. B. Mazulquim, K. J. Lee, J. W. Yoon, L. V. Muniz, B.-H. V. Borges, L. G. Neto, and R. Magnusson, "Efficient band-pass color filters enabled by resonant modes and plasmons near the Rayleigh anomaly," *Opt. Express*, vol. 22, no. 25, pp. 30843–30851, Dec. 2014.
[35] S. He, Z. Shi, X. Li, X. Gao, Z. Wang, Q. Liu, G. Zhu, M. Zhang, H. Zhu, and Y. Wang, "Membrane guided-mode resonant color filters exhibiting adjustable spectral response," *Opt. Commun.*, vol. 342, pp. 129–135, May 2015.
[36] K. Luke, Y. Okawachi, M. R. E. Lamont, A. L. Gaeta, M. Lipson, "Broadband mid-infrared frequency comb generation in a Si_3N_4 microresonator," *Opt. Lett.*, vol. 40, no. 21, pp. 4823–4826, Nov. 2015.
[37] I. H. Malitson, "Interspecimen comparison of the refractive index of fused silica," *J. Opt. Soc. Am.*, vol. 55, no. 10, pp. 1205–1209, Oct. 1965.
[38] M. Daimon and A. Masumura, "Measurement of the refractive index of distilled water from the near-infrared region to the ultraviolet region," *Appl. Opt.*, vol. 46, no. 18, pp. 3811–3820, June 2007.
[39] Y. Zhou, M. C. Y. Huang, and C. J. Chang-Hasnain, "Large fabrication tolerance for VCSELs using high-contrast grating," *IEEE Photonics Technol. Lett.*, vol. 20, no. 6, pp. 434–436, Mar. 2008.

Yuusuke Takashima received his PhD degree from Tokushima University, Japan, in 2017. Since February 2019, he has been a research associate researcher at Tokushima University. Recently, his research interest has been focused on subwavelength structures and their photonic applications.

Keita Kusaba graduated Tokushima University, Japan, in 2016, and received his M.S. degree from Tokushima University in 2018. His research interest is applications of sensing devices with nano periodic structure.

Masanobu Maraguchi received his PhD degree from Osaka University in 1993. Since 2009, he has been a professor at Tokushima University. He is interested in the characteristics and applications of localized and propagating plasmons on nanometal structures. Recently, his main interests have been channel-type plasmonic waveguides, their applications, and a split-ring resonator for the infrared and visible regions.

Yoshiki Naoi is a professor at Tokushima University, Japan. He graduated Tokushima University and Tohoku University, Japan, in 1988 and 1993, respectively, and received his PhD degree from Tohoku University in 1993. His research interest is focused on optical engineering and photonic device